Check for updates

ORIGINAL PAPER

physica status solidi b
www.pss-b.com

Reducing the Impact of Bulk Doping on Transport Properties of Bi-Based 3D Topological Insulators

*Shaham Jafarpisheh, An Ju, Kevin Janßen, Takashi Taniguchi, Kenji Watanabe, Christoph Stampfer, and Bernd Beschoten**

The observation of helical surface states in Bi-based 3D topological insulators (TIs) has been a challenge since their theoretical prediction. The main issue arises when the Fermi level shifts deep into the bulk conduction band due to unintentional doping. This results in the metallic conduction of the bulk which dominates the transport measurements and hinders the probing of the surface states in these experiments. Here, various strategies are investigated to reduce the residual doping in Bi-based TIs. Flakes of Bi_2Se_3 and $Bi_{1.5}Sb_{0.5}Te_{1.7}Se_{1.3}$ are grown by physical vapor deposition and their structural and electronic properties are compared with mechanically exfoliated flakes. Using Raman spectroscopy, the role of the substrate in this process is explored, and the optimal conditions for the fabrication of high-quality crystals are presented. Despite this improvement, it is shown that the vapor phase-deposited flakes still suffer from structural disorder which leads to the residual n-type doping of the bulk. Using magneto-transport measurements, we find that exfoliated flakes show better electrical properties and are thus more promising for the probing of surface states.

1. Introduction

The relevance of topology in the electronic properties of materials gives rise to the concept of topological insulators (TIs), which is a fascinating frontier in condensed matter physics.[1–3] The nontrivial band structure of these materials ensures the presence of gapless surface states with a helical spin texture where the spin orientation of the electrons is locked to their momentum direction. Therefore, as long as the time-reversal symmetry is preserved, electrons are protected against backscattering. Such dissipationless current can improve the efficiency of electronics and is highly desired for future spintronic and photonic devices.[4,5] Since the first experimental confirmation of 2D TIs in 2007,[6] extensive effort has been directed toward the observation of surface states in 3D systems using electrical transport measurements.[7–18] However, the challenge remains due to the parallel conduction of the bulk states in 3D crystals and the development of a reliable method to distinguish the contribution of surface states in electrical conduction. Unintentional doping of 3D TIs, specifically in Bi-based compounds, places the Fermi level deep inside the bulk conduction band. This results in the metallic conduction of the bulk states instead of a semiconducting behavior expected from the gap band structure. A step forward is to analyze the source of this doping and improve the fabrication process with the goal of reducing the bulk contribution to electrical transport.

In this study, we present the vapor phase deposition of Bi-based TIs on various substrates including SiO_2, hexagonal boron nitride (hBN), and graphene (Gr). We present a systematic thickness-dependent Raman spectroscopy study to gain insight into the role of the substrate for the structural disorder of fabricated crystals. Next, several approaches to improve the transport properties of 3D TIs are discussed in detail.

2. Physical Vapor Deposition

Vapor phase growth is a robust technique for the fabrication of TIs on various substrates with desired thicknesses and forms.[19–23] In this technique, the source material is heated to elevated temperatures and slowly evaporates during the growth process. An inert carrier gas such as Ar carries the evaporated material onto the deposition substrates. The lower temperature in this region results in a highly controllable deposition process. **Figure 1**a shows a schematic view of the growth chamber which is used in this study. The source crystal is heated to a temperature of $T \approx 600–700\,°C$, whereas the substrates are placed at a lower temperature of $T \approx 300–350\,°C$.

By optimizing the growth process, highly crystalline flakes can be grown on various substrates including SiO_2, hBN, and Gr, as shown in Figure 1b. Independent of the particular substrate,

---

S. Jafarpisheh, A. Ju, K. Janßen, C. Stampfer, B. Beschoten
2nd Institute of Physics and JARA-FIT
RWTH Aachen University
52074 Aachen, Germany
E-mail: bernd.beschoten@physik.rwth-aachen.de

S. Jafarpisheh, C. Stampfer
Peter Grünberg Institute (PGI-9)
Forschungszentrum Jülich
52425 Jülich, Germany

T. Taniguchi, K. Watanabe
National Institute for Materials Science
1-1 Namiki, Tsukuba 305-0044, Japan

The ORCID identification number(s) for the author(s) of this article can be found under https://doi.org/10.1002/pssb.202000021.

© 2020 The Authors. Published by WILEY-VCH Verlag GmbH & Co. KGaA, Weinheim. This is an open access article under the terms of the Creative Commons Attribution License, which permits use, distribution and reproduction in any medium, provided the original work is properly cited.

DOI: 10.1002/pssb.202000021

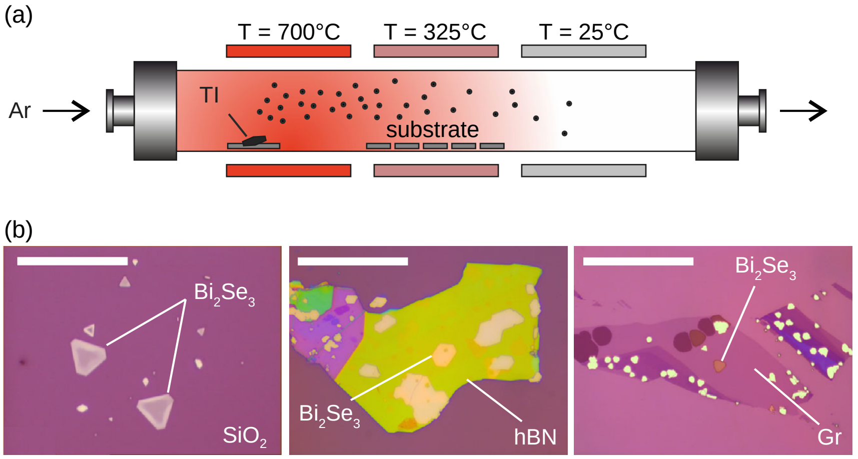

Figure 1. a) Schematic of the three-zone furnace which is used to deposit thin TI flakes on various substrates. b) Growth of Bi_2Se_3 flakes with thicknesses in the range of 1–50 nm on SiO_2, hBN, and Gr. The scale bars correspond to a length of 10 μm.

there is a huge spread in the thicknesses of the deposited crystals ranging from 1 to 300 nm in a single run. While this growth mode is favorable when studying thickness-dependent structural properties (see next section), it does not allow synthesizing large-area flakes with a controlled number of layers. We note that higher control over the layer number can be achieved for ultrathin flakes using solution-based growth methods.[24,25] Our physical vapor deposition (PVD) technique does not require any catalyst for deposition which reduces one source of contamination in the process. However, the rough surface of SiO_2 can induce structural defects in TI crystal and increase the doping level of the bulk.[20] One solution is to grow free-standing flakes with minimum contact to the substrate which can reduce the impact of the SiO_2 surface.[19] In this method, however, both surfaces of the TI are exposed to air and water vapor when the flakes are removed from the growth chamber, which can significantly increase unintentional doping. An alternative is the use of hBN as a substrate, which offers an atomically flat surface.[26] In this approach, the hBN flakes are exfoliated onto Si/SiO_2 substrate prior to the PVD process. Next, TI flakes are grown by PVD directly on hBN (Figure 1b, middle). Thickness-dependent color contrasts of optical images, which result from the interference of the reflected light of the flakes, can be used to identify suitable crystals for transport measurements. This is shown in **Figure 2**a where the color of TI flakes changes from dark blue for ultrathin crystals to yellow for thicker ones, as confirmed by atomic force microscopy (AFM) scans (Figure 2b,c). Therefore, TI flakes with the desired thicknesses can directly be identified after PVD

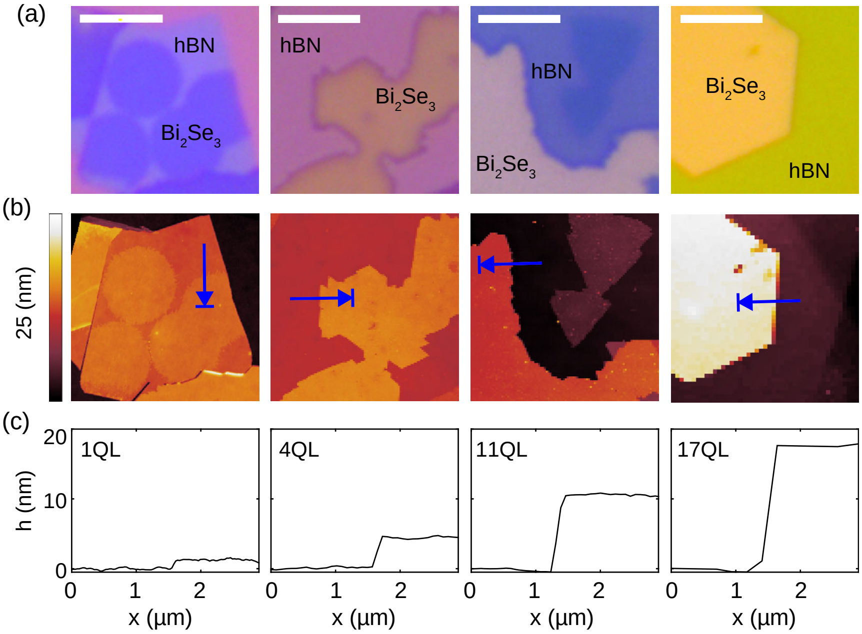

Figure 2. a) Optical images of Bi_2Se_3 flakes grown with various thicknesses on exfoliated hBN. b) AFM scan of the flakes shown in (a). c) AFM line scan at the edge of the flakes as it is shown in (b), showing the thickness (scale bars are 4 μm).

© 2020 The Authors. Published by WILEY-VCH Verlag GmbH & Co. KGaA, Weinheim

growth without the need of an additional AFM scan. This significantly reduces the air exposure time prior to both processing and transport measurements.

3. Thickness-Dependent Raman Spectroscopy

Bi_2Se_3 has a rhombohedral crystal structure with four Raman active modes, two in-plane (E_g) and two out-of-plane (A_g) modes. **Figure 3**a shows a typical Raman spectrum of the PVD-fabricated flakes with $E_g^1 \approx 37\,cm^{-1}$, $E_g^2 \approx 131\,cm^{-1}$, $A_{1g}^1 \approx 72\,cm^{-1}$, and $A_{1g}^2 \approx 174\,cm^{-1}$ confirming the composition of the deposited flakes.[27–29] The thickness dependency of these Raman modes provides information on the structural properties of the layer and is a tool to identify the role of the substrate.[27] Specifically, we observed that the the strain induced in the TI crystal structure as a result of the surface roughness of SiO_2 can penetrate several nanometers more than that of hBN.

Figure 3b shows the evolution of the Raman spectra of the Bi_2Se_3 flake on hBN with decreasing thicknesses ranging from around 300 to 1 quintuple layer (1 QL ≈ 1 nm). The intensities of all spectra are normalized by their A_{1g}^2 mode and shifted vertically for clarity. By fitting Lorentzian line shapes, the positions of each Raman peak are extracted and plotted as a function of the thickness in Figure 3c,d. The redshift in A_{1g}^1 and E_g^2 modes in addition to the blueshift in A_{1g}^2 for thicknesses lower than ≈10 nm is consistent with previous reports.[29–31] This shift for thin flakes could be either due to phonon confinement or due to strain induced from the interface between the flakes and the substrate. Phonon confinement in thin flakes is expected to mainly affect the out-of-plane vibrational modes, whereas a stronger effect on the in-plane modes is expected from the substrate-induced strain. Based on our observations, the peak position of the in-plane mode (E_g^2 in Figure 3d) is affected more strongly than the respective positions of the out-of-plane modes (A_{1g}^1 and A_{1g}^2 in Figure 3c,e). This suggests that the strain from the substrate plays a more important role in the structural changes of thinner flakes. The red shift of E_g^2 and the blue shift of A_{1g}^2 are the results of tensile strain in the lattice structure of Bi_2Se_3. The strain resulting from the hBN substrate penetrates 5–6 nm inside the flakes. However, the penetration depth in flakes deposited on SiO_2 is ≈3–4 nm larger as shown by comparing the red and green dots in Figure 3c. This is a direct consequence of SiO_2 roughness and surface inhomogeneities which lead to less screening from the underlying QLs.

Comparing the electrical conductivity of Bi_2Se_3 on the two surfaces further illustrates the crucial role of the substrate for doping concentration in the TI. Using conventional lithography techniques, Cr/Au contacts were fabricated on two typical flakes deposited on hBN and SiO_2 substrates. As the TI flakes were grown free standing on the SiO_2 substrate, an initial transfer process was necessary to achieve flakes lying flat on the surface. This step is not required for the TIs grown on hBN which results in a cleaner process. Comparing the resistances of the two devices, we could observe a larger backgate tunability of the TI grown on hBN substrate (compare the percentage change in resistance, as shown by the red and green traces in Figure 3f). This is a clear indication that the Fermi level of TI/hBN is closer to the bottom edge of the bulk conduction band and indicates an improvement in the overall transport properties of the TI layer.

4. Quaternary TIs

A promising approach to reduce the large bulk conductivity of binary bismuth-based TIs is the use of quaternary compounds composed of Bi, Sb, Te, and Se (BSTS). In these materials, negatively charged Se vacancies are compensated by positively charged Te antisites when an optimum composition is used. This has been shown to result in a suppression of bulk residual doping.[32,33] Furthermore, angle-resolved photoemission spectroscopy (ARPES) measurements have shown no observable Rashba splitting in BSTS compounds unlike Bi_2Se_3.[33–35] This is an advantage of BSTS as it is a challenge to distinguish the

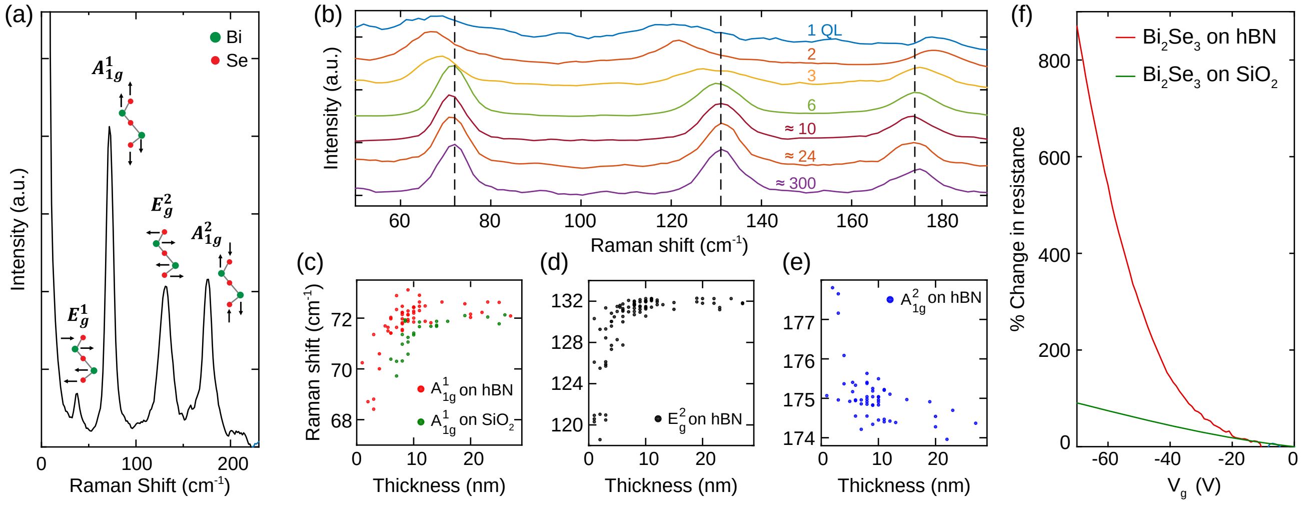

Figure 3. a) A typical Raman spectrum of Bi_2Se_3 and schematic view of each vibrational mode. b) Thickness-dependent Raman spectra of Bi_2Se_3. c,d) Peak positions extracted using Lorentzian fits of the Raman signals for c) A_{1g}^1, d) E_g^2, and e) A_{1g}^2 vibrational modes. f) Four-probe resistance as a function of backgate voltage for Bi_2Se_3 deposited on hBN and SiO_2. Both flakes have similar thicknesses of around ≈10 nm.

© 2020 The Authors. Published by WILEY-VCH Verlag GmbH & Co. KGaA, Weinheim

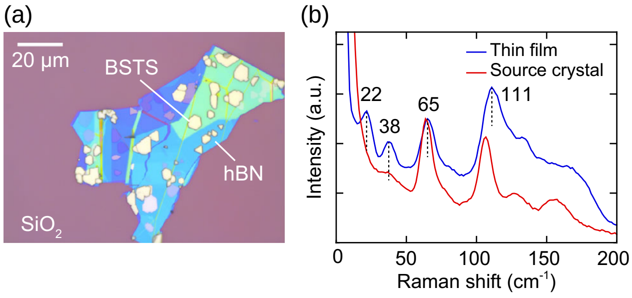

Figure 4. a) An optical image of BSTS grwon on hBN using the PVD process. b) Raman spectra of the source crystal used in the PVD process and the deposited thin film.

contribution of the Rashba states from the topologically protected states in transport measurements.

We use the PVD method to deposit thin BSTS flakes on hBN. **Figure 4**a shows an optical image of such flakes with flat edges which indicate a high crystal quality. Raman spectroscopy can be used to compare the composition of the deposited thin films and the evaporation source material used in this process (Figure 4b). As confirmed by energy dispersive X-ray spectroscopy (EDX) measurements (not shown), the source crystals have the composition of $Bi_{1.5}Sb_{0.5}Te_{1.7}Se_{1.3}$. While the EDX analysis could not be conducted on thin crystals, the similar peak positions of the Raman spectra for the deposited BSTS crystals shown in Figure 4b reveal a comparable composition. The difference between the two spectra is resulted from the thickness-dependent shift of the frequencies similar to our observations in Figure 3 for Bi_2Se_3 and the measurements reported in the study by Tu et al.[36] for BSTS. As the air exposure after deposition can still lead to degradation and doping of the flakes, the top surface of the layers is covered by dry transferring another hBN flake immediately after the PVD process. This further ensures the protection of the flakes during the fabrication process of electrical contacts. **Figure 5**a shows an AFM image of a thin BSTS encapsulated in two hBN flakes. To electrically access the TI layer, reactive ion etching (RIE) is used to pattern a Hall bar shape through the stack. In this context, it is important to select the etching process gas which allows for high selectivity on hBN and TI etching while having a minimum effect on the SiO_2 layer as the strong etching of the SiO_2 layer leads to an unstable back gate during the electrical measurements. After testing various process gases, Ar and CHF_3 are found to be the most suitable mixture. As shown in Figure 5b, lower applied RF powers results in similar etching rates of the three layers which are preferential compared with high powers for which SiO_2 and hBN are etched at much higher rates compared with the TI layer. The schematic and optical view of the final device are shown in Figure 5d,e. This fabrication process indeed improved the transport properties of TI layers. Figure 5c shows the charge carrier densities extracted from the Hall effect measurements for both a fully encapsulated BSTS crystal (hBN/BSTS/hBN) (blue data points) and a Bi_2Se_3/hBN half sandwich (red data points). The charge carrier density of the bulk states is reduced by one order of magnitude (compare blue with red data points). As a result, the backgate tunability of the BSTS flake has significantly improved, as shown in Figure 5f.

The magnetoconductivity measurements of this device also indicate an improvement of the transport properties. **Figure 6**a shows conductivity as a function of the perpendicular magnetic field at different backgate voltages. Detailed analysis of conductivity provides an insight into the role of bulk states to the

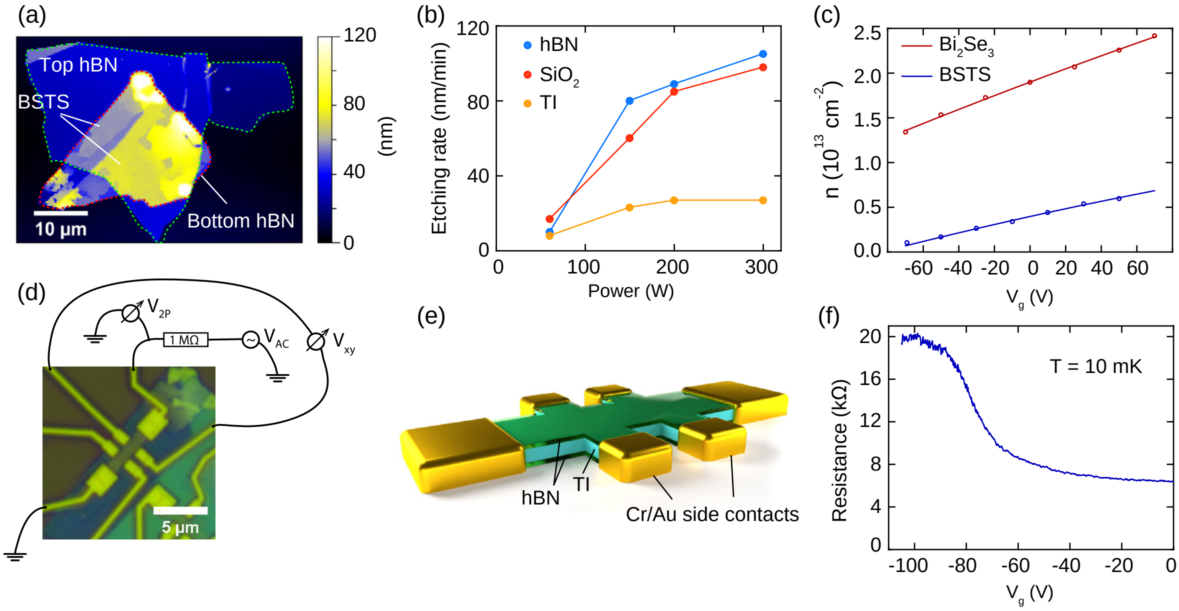

Figure 5. a) An AFM scan of a PVD-grown BSTS encapsulated in hBN. b) Etching rates of TI, SiO_2, and hBN at different RIE powers using CHF_3 and Ar gas mixture. c) Charge carrier density of Bi_2Se_3 and BSTS as a function of backgate voltage extracted from Hall measurements. Measurements are carried out at $T = 1$ K for Bi_2Se_3 and $T = 10$ mK for BSTS. d) Schematic view of measurement configuration of an encapsulated BSTS Hall bar. e) View of fully encapsulated TI in hBN and fabricated edge contacts. f) Four-probe resistance of BSTS as a function of backgate.

© 2020 The Authors. Published by WILEY-VCH Verlag GmbH & Co. KGaA, Weinheim

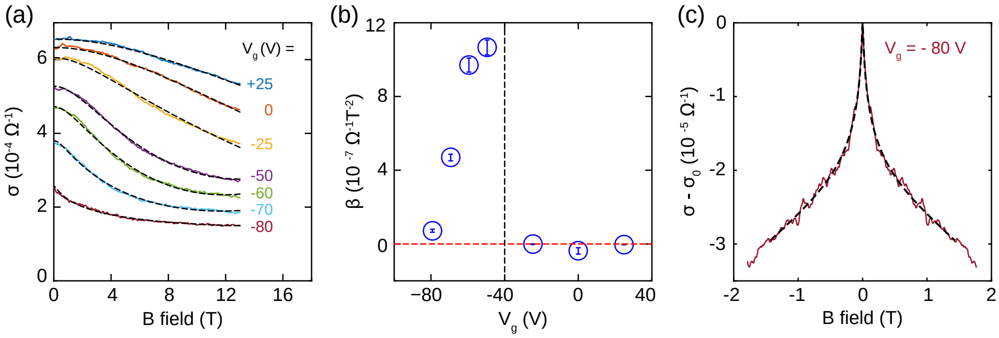

Figure 6. a) Magnetoconductivity trace of BSTS device measured at different backgate voltages (V_g). The black dashed lines show the modified HLN model. b) The value of β extracted from the HLN fits. The red and black dashed lines indicate $\beta = 0$ and $V_g = -40$ V, respectively. c) WAL cusp measured at a backgate voltage of $V_g = -80$ V. The black dashed line of the fit using HLN model.

transport. The conductivity of the materials with large spin-orbit coupling as a function of magnetic field can be described by the Hikami–Larkin–Nagaoka (HLN) model given as[37]

$$\Delta\sigma = \frac{\alpha e^2}{2\pi^2\hbar}\left[\ln\left(\frac{\hbar}{4Bel_\phi^2}\right) - \Psi\left(\frac{1}{2}+\frac{\hbar}{4Bel_\phi^2}\right)\right] + \beta B^2 \qquad (1)$$

Here, α is a fitting prefactor, l_ϕ is the phase coherence length, ψ is the digamma function, and B is the external magnetic field. The coefficient of the quadratic term (β) describes additional scattering terms at high magnetic fields and consists of a quantum correction part (β_q) and a classical part (β_c) as $\beta = \beta_q + \beta_c$. The quantum correction term can be described by the following expression[37,38]

$$\beta_q = \frac{-e^2}{48\pi^2\hbar}\left[\frac{1}{B_{SO}+B_e}\right]^2 + \frac{3e^2}{96\pi^2\hbar}\left[\frac{1}{(4/3)B_{SO}+B_\phi}\right]^2 \qquad (2)$$

with $B_{SO,e,\phi} = \hbar/(4el_{SO,e,\phi}^2)$. The relative values of both the spin-orbit (l_{SO}) and elastic scattering (l_e) length scales determine the sign of the quantum correction coefficient. In materials with large spin-orbit coupling such as TIs, the B_{SO} term ensures the positive sign of β_q based on Equation (2). In contrast, the classical part has a negative sign and can be written as[38,39]

$$\beta_c = -\mu_{GMR}^2\sigma_0 \qquad (3)$$

Here μ_{GMR} is the geometrical magnetoresistance mobility, $\mu_{GMR} = \xi\mu_H$ with μ_H being the Hall mobility, and ξ is the magnetoresistance scattering factor.[39] Therefore, the sign of the quadratic term in Equation (1) indicates whether the classical term and therefore bulk states dominate over the transport. Figure 6b shows the values of β extracted from the fits indicated by the dashed lines in Figure 6a at different backgate voltages. The negative value at zero backgate voltage shows the dominance of bulk transport contributions. However, the sign of β becomes positive for negative backgate voltages, which is consistent to the lowering of the Fermi energy and a suppression of the bulk conduction channel. This can also qualitatively be seen in Figure 6a by comparing the curvature of the magnetoconductivity traces at high magnetic fields at $V_g = -25$ V (yellow curve) and $V_g = -50$ V (purple curve). Further increase in the backgate voltage results in smaller values of β. This is due to the development of the weak antilocalization (WAL) signal which becomes dominant at very low magnetic fields (Figure 6c) and as a result, the first term of Equation (1) gains importance in the fitting procedure. The result of this fit is shown by the dashed line in Figure 6c. Nevertheless, the curvature of magnetoconductivity at $V_g = -80$ V is completely different from $V_g = +25$ V, which shows that in these materials, it is possible to reduce the contribution of the bulk states using electric gate fields. This is in contrast to Bi_2Se_3 where the linear magnetoconductivity is typically observed at all gate voltages (**Figure 7**a). Despite these overall improvements, the PVD-grown quaternary TIs still exhibit residual bulk doping. This might also result from large-scale structural defects which occur during the deposition process, as observed in epitaxial TI films.[40]

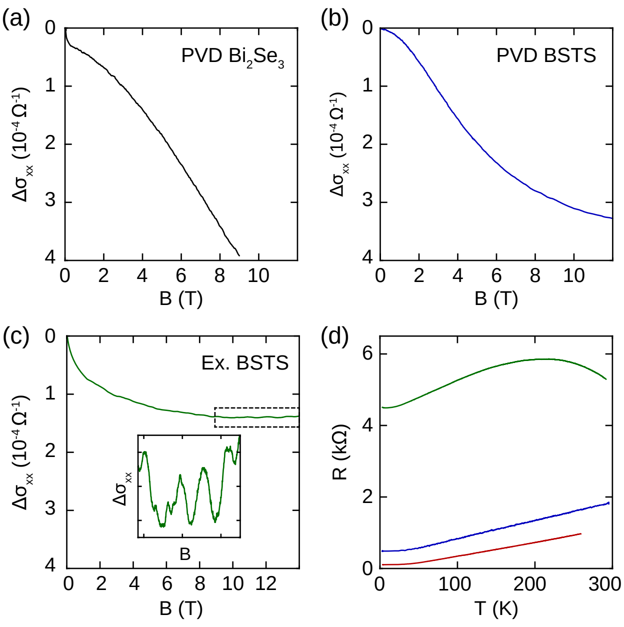

Figure 7. Magnetoconductivity of a) PVD Bi_2Se_3, b) PVD BSTS, and c) exfoliated BSTS flakes. d) Temperature dependency of the resistance for material systems shown in panels (a)–(c).

5. Exfoliation

Although the PVD method could be important for the fabrication of larger-scale TI crystals, it still has major limitations. In comparison with the solution-based methods, PVD offers a lower control over the number of the layers.[25] Furthermore, despite major improvements of the transport properties using quaternary encapsulated PVD layers, exfoliated flakes from single crystals still exhibit the highest electronic quality.

A direct comparison of the transport properties of Bi_2Se_3 and BSTS flakes fabricated by PVD and an exfoliated BSTS flake is shown in Figure 7. As mentioned earlier, the PVD-fabricated Bi_2Se_3 (Figure 7a) typically shows a classical linear magnetoconductivity at large magnetic fields due to the large bulk charge carrier densities.[19,41] The dominance of bulk transport can also be observed in the temperature-dependent resistance of PVD Bi_2Se_3 which shows a metallic behavior in the entire range of the measurements (see the red trace in Figure 7d). Using BSTS as the source material in the PVD process improves transport properties, as discussed in the previous section. The temperature dependency of the resistance in these types of devices is still metallic but with higher resistances. However, the magnetoresistance at high magnetic fields shows quadratic dependency, as shown in Figure 7b, which suggests the decoupling of bulk from the surface states.[42] In contrast, a major improvement of the transport properties is observed when using the exfoliation technique. The absence of structural defects resulting from the PVD process leads to a lower bulk charge carrier concentration, a larger Hall mobility reaching 4500 $cm^2\,(V\,s)^{-1}$ (compared with typical values lower than 1000 $cm^2\,(V\,s)^{-1}$ for PVD-grown crystals), and the observation of the quantum oscillations at high magnetic fields (inset of Figure 7c). Furthermore, the semiconducting temperature dependency of the resistance at temperatures close to room temperature (see the yellow trace in Figure 7d at $T > 200$ K) also indicates a smaller bulk contribution in the transport.

We conclude that exfoliated BSTS TIs provide the most suitable material to explore the transport properties of the topologically protected surface states. However, even for this material, it is not easily possible to separate the remaining contribution of bulk states in the measurements such as WAL or the Shubnikov de Haas (SdH) oscillations. In fact, extracting a π-Berry phase from the analysis of high B-field quantum oscillations with the goal of indicating surface transport can be misleading.[7–10,12–14] Based on the study conducted by Kuntsevich and coworkers,[43] other mechanisms such as sample inhomogeneities and a magnetic field dependence of the chemical potential can result in a phase shift similar to what is expected from the surface states. In contrast, the uncertainty in such analysis is much larger than the extracted values for the phase of SdH oscillations. Alternatively, spin-sensitive potentiometric measurements are carried out in which ferromagnetic electrodes are used to directly detect the spin polarization of the surface current.[44,45] Carrying out these types of measurements in a nonlocal detection scheme makes it possible to separate the contribution of the bulk and solely characterize the topologically protected surface states.[46]

6. Conclusions

In summary, the fabrication of Bi-based TIs using PVD and exfoliation techniques is discussed in detail. The quality of the crystals and the impact of the substrates have been analyzed using Raman spectroscopy measurements. Exfoliation from bulk crystals has been identified as a more suitable approach for studying the surface states of TIs compared with samples deposited by the PVD process.

Acknowledgements

This work was supported by the Deutsche Forschungsgemeinschaft (DFG, German Research Foundation) via SPP 1666 (BE 2441/8) and under Germanys Excellence Strategy—Cluster of Excellence “Matter and Light for Quantum Computing” (ML4Q) EXC 2004/1-390534769, the European Unions Horizon 2020 research and innovation programme under grant agreement no. 785219 (Graphene Flagship), the Virtual Institute for Topological Insulators (Jülich–Aachen–Würzburg–Shanghai), and the Helmholtz Nano Facility[47] at the Forschungszentrum Jülich. The growth of hexagonal boron nitride crystals was supported by the Elemental Strategy Initiative conducted by MEXT, Japan, A3 Foresight by JSPS, and the CREST (grant no. JPMJCR15F3), JST. Open access funding enabled and organized by Projekt DEAL.

Conflict of Interest

The authors declare no conflict of interest.

Keywords

Bi_2Se_3, Bi–Sb–Te–Se compounds, graphene, surface states, topological insulators, vapor phase deposition

Received: January 13, 2020
Revised: February 27, 2020
Published online: March 23, 2020

[1] J. M. Kosterlitz, D. J. Thouless, *J. Phys. C: Solid State Phys.* **1973**, *6*, 1181.
[2] C. L. Kane, E. J. Mele, *Phys. Rev. Lett.* **2005**, *95*, 146802.
[3] C. L. Kane, E. J. Mele, *Phys. Rev. Lett.* **2005**, *95*, 226801.
[4] P. Yan, R. Lin, H. Chen, H. Zhang, A. Liu, H. Yang, S. Ruan, *IEEE Photonics Technol. Lett.* **2014**, *27*, 264.
[5] S. K. Ivanov, Y. Zhang, Y. V. Kartashov, D. V. Skryabin, *APL Photonics* **2019**, *4*, 126101.
[6] M. König, S. Wiedmann, C. Brüne, A. Roth, H. Buhmann, L. W. Molenkamp, X. L. Qi, S. C. Zhang, *Science* **2007**, *318*, 766.
[7] D. X. Qu, Y. S. Hor, J. Xiong, R. J. Cava, N. P. Ong, *Science* **2010**, *329*, 821.
[8] J. G. Analytis, R. D. McDonald, S. C. Riggs, J. H. Chu, G. S. Boebinger, I. R. Fisher, *Nat. Phys.* **2010**, *6*, 960.
[9] Z. Ren, A. A. Taskin, S. Sasaki, K. Segawa, Y. Ando, *Phys. Rev. B* **2010**, *82*, 241306.
[10] A. A. Taskin, Z. Ren, S. Sasaki, K. Segawa, Y. Ando, *Phys. Rev. Lett.* **2011**, *107*, 016801.
[11] Y. S. Kim, M. Brahlek, N. Bansal, E. Edrey, G. A. Kapilevich, K. Iida, M. Tanimura, Y. Horibe, S. W. Cheong, S. Oh, *Phys. Rev. B* **2011**, *84*, 073109.
[12] B. Sacépé, J. B. Oostinga, J. Li, A. Ubaldini, N. J. G. Couto, E. Giannini, A. F. Morpurgo, *Nat. Commun.* **2011**, *2*, 1.

© 2020 The Authors. Published by WILEY-VCH Verlag GmbH & Co. KGaA, Weinheim

[13] J. Xiong, Y. Luo, Y. Khoo, S. Jia, R. J. Cava, N. P. Ong, *Phys. Rev. B* **2012**, *86*, 045314.
[14] A. A. Taskin, S. Sasaki, K. Segawa, Y. Ando, *Phys. Rev. Lett.* **2012**, *109*, 066803.
[15] N. Bansal, Y. S. Kim, M. Brahlek, E. Edrey, S. Oh, *Phys. Rev. Lett.* **2012**, *109*, 116804.
[16] D. Kim, P. Syers, N. P. Butch, J. Paglione, M. S. Fuhrer, *Nat. Commun.* **2013**, *4*, 1.
[17] C. Weyrich, M. Drögeler, J. Kampmeier, M. Eschbach, G. Mussler, T. Merzenich, T. Stoica, I. E. Batov, J. Schubert, L. Plucinski, B. Beschoten, C. M. Schneider, C. Stampfer, D. Grützmacher, T. Schäpers, *J. Phys.: Condens. Matter* **2016**, *28*, 495501.
[18] P. Seifert, K. Vaklinova, K. Kern, M. Burghard, A. Holleitner, *Nano Lett.* **2017**, *17*, 973.
[19] R. Ockelmann, A. Müller, J. H. Hwang, S. Jafarpisheh, M. Drögeler, B. Beschoten, C. Stampfer, *Phys. Rev. B* **2015**, *92*, 085417.
[20] P. Gehring, B. F. Gao, M. Burghard, K. Kern, *Nano Lett.* **2012**, *12*, 5137.
[21] W. Dang, H. Peng, H. Li, P. Wang, Z. Liu, *Nano Lett.* **2010**, *10*, 2870.
[22] Y. Yan, Z. M. Liao, Y. B. Zhou, H. C. Wu, Y. Q. Bie, J. J. Chen, J. Meng, X. S. Wu, D. P. Yu, *Sci. Rep.* **2013**, *3*, 1.
[23] D. Kong, J. C. Randel, H. Peng, J. J. Cha, S. Meister, K. Lai, Y. Chen, Z. X. Shen, H. C. Manoharan, Y. Cui, *Nano Lett.* **2010**, *10*, 329.
[24] Y. Min, G. D. Moon, B. S. Kim, B. Lim, J. S. Kim, C. Y. Kang, U. Jeong, *J. Am. Chem. Soc.* **2012**, *134*, 2872.
[25] H. Xie, Z. Li, Z. Sun, J. Shao, X. F. Yu, Z. Guo, J. Wang, Q. Xiao, H. Wang, Q. Q. Wang, H. Zhang, P. K. Chu, *Small* **2016**, *12*, 4136.
[26] J. Xue, J. Sanchez-Yamagishi, D. Bulmash, P. Jacquod, A. Deshpande, K. Watanabe, T. Taniguchi, P. Jarillo-Herrero, B. J. LeRoy, *Nat. Mater.* **2011**, *10*, 282.
[27] K. M. F. Shahil, M. Z. Hossain, V. Goyal, A. A. Balandin, *J. Appl. Phys.* **2012**, *111*, 054305.
[28] W. Richter, C. R. Becker, *Phys. Status Solidi B* **1977**, *84*, 619.
[29] J. Zhang, Z. Peng, A. Soni, Y. Zhao, Y. Xiong, B. Peng, J. Wang, M. S. Dresselhaus, Q. Xiong, *Nano Lett.* **2011**, *11*, 2407.
[30] C. Wang, X. Zhu, L. Nilsson, J. Wen, G. Wang, X. Shan, Q. Zhang, S. Zhang, J. Jia, Q. Xue, *Nano Res.* **2013**, *6*, 688.
[31] S. Xu, Y. Han, X. Chen, Z. Wu, L. Wang, T. Han, W. Ye, H. Lu, G. Long, Y. Wu, J. Lin, Y. Cai, K. M. Ho, Y. He, N. Wang, *Nano Lett.* **2015**, *15*, 2645.
[32] Z. Ren, A. A. Taskin, S. Sasaki, K. Segawa, Y. Ando, *Phys. Rev. B* **2011**, *84*, 165311.
[33] T. Arakane, T. Sato, S. Souma, K. Kosaka, K. Nakayama, M. Komatsu, T. Takahashi, Z. Ren, K. Segawa, Y. Ando, *Nat. Commun.* **2012**, *3*, 1.
[34] M. Neupane, S. Y. Xu, L. A. Wray, A. Petersen, R. Shankar, N. Alidoust, C. Liu, A. Fedorov, H. Ji, J. M. Allred, Y. S. Hor, T. R. Chang, H. T. Jeng, H. Lin, A. Bansil, R. J. Cava, M. Z. Hasan, *Phys. Rev. B* **2012**, *85*, 235406.
[35] P. D. C. King, R. C. Hatch, M. Bianchi, R. Ovsyannikov, C. Lupulescu, G. Landolt, B. Slomski, J. H. Dil, D. Guan, J. L. Mi, E. D. L. Rienks, J. Fink, A. Lindblad, S. Svensson, S. Bao, G. Balakrishnan, B. B. Iversen, J. Osterwalder, W. Eberhardt, F. Baumberger, Ph. Hofmann, *Phys. Rev. Lett.* **2011**, *107*, 096802.
[36] N. H. Tu, Y. Tanabe, K. K. Huynh, Y. Sato, H. Oguro, S. Heguri, K. Tsuda, M. Terauchi, K. Watanabe, K. Tanigaki, *Appl. Phys. Lett.* **2014**, *105*, 063104.
[37] S. Hikami, A. I. Larkin, Y. Nagaoka, *Prog. Theor. Phys.* **1980**, *63*, 707.
[38] B. A. Assaf, T. Cardinal, P. Wei, F. Katmis, J. S. Moodera, D. Heiman, *Appl. Phys. Lett.* **2013**, *102*, 012102.
[39] D. K. Schroder, *Semiconductor Materials Devices Characterization*, Wiley-Interscience, Hoboken, NJ, **2006**.
[40] D. R. Hickey, R. J. Wu, J. S. Lee, J. G. Azadani, R. Grassi, D. C. Mahendra, J.-P. Wang, T. Low, N. Samarth, K. A. Mkhoyan, *Phys. Rev. Mater.* **2020**, *4*, 011201(R).
[41] J. Hu, T. F. Rosenbaum, *Nat. Mater.* **2008**, *7*, 697.
[42] S. Singh, R. K. Gopal, J. Sarkar, A. Pandey, B. G. Patel, C. Mitra, *J. Phys.: Condens. Matter* **2017**, *29*, 505601.
[43] A. Yu, A. V. Shupletsov Kuntsevich, G. M. Minkov, *Phys. Rev. B* **2018**, *97*, 195431.
[44] P. Schwab, R. Raimondi, C. Gorini, *Europhys. Lett.* **2011**, *93*, 67004.
[45] C. H. Li, O. M. J. van't Erve, J. T. Robinson, Y. Liu, L. Li, B. T. Jonker, *Nat. Nanotechnol.* **2014**, *9*, 218.
[46] S. Jafarpisheh, F. Volmer, Z. Wang, B. Canto, Y. Ando, C. Stampfer, B. Beschoten, arXiv:1907.10347, **2019**.
[47] W. Albrecht, J. Moers, B. Hermanns, *J. Large-Scale Res. Facil.* **2017**, *3*, A112.

© 2020 The Authors. Published by WILEY-VCH Verlag GmbH & Co. KGaA, Weinheim